Earth and Planetary Science Letters 287 (2009) 130–136

Contents lists available at ScienceDirect

Earth and Planetary Science Letters

journal homepage: www.elsevier.com/locate/epsl

Evidence and implications of crustal magmatism on the flanks of the East Pacific Rise

D. Troy Durant *, Douglas R. Toomey

Department of Geological Sciences, 1272 University of Oregon, Eugene, Oregon 97403-1272, USA

ARTICLE INFO

Article history:
Received 5 March 2009
Received in revised form 16 July 2009
Accepted 5 August 2009
Available online 8 September 2009

Editor: R.D. van der Hilst

Keywords:
East Pacific Rise
mid-ocean ridge
oceanic crust
off-axis magmatism
waveform modeling

ABSTRACT

Formation of oceanic crust along the East Pacific Rise is thought to be complete within a few kilometers of the rise axis. Here, however, we present evidence for magmatism 20 km from the spreading center in 300-ka-old crust. Seismic data reveal an intrusive complex ~2 km beneath the seafloor, which is limited in lateral extent (<5 km) and comprises a melt lens underlain by low-velocity, high-attenuation crust. The crustal magma body overlies a region of off-axis delivery of mantle melt that results from a long-lived skew between the axes of mantle upwelling and plate spreading. Magmatism on the flanks of the EPR may be commonplace, thus affecting the architecture of oceanic crust and providing the necessary conditions to drive off-axis hydrothermal activity.

1. Introduction

Crustal accretion along the fast-spreading East Pacific Rise (EPR) occurs primarily within a narrow cross-axis window centered on the axis of plate spreading. Seafloor mapping shows that the eruptive fissures defining the neovolcanic zone occur within a kilometer-wide region centered on the axial high (Haymon et al., 1991; Macdonald and Fox, 1988; Fornari et al., 1998). Geophysical studies further reveal that directly beneath the axial high lies a narrow, steep-sided, crustal magma chamber and a seismically detectable crust-mantle transition zone or Moho (Detrick et al., 1987; Kent et al., 1990; Dunn et al., 2000). These observations have been used to infer that mantle melt is efficiently focused beneath the rise axis and that the emplacement of crust is effectively complete at zero age (e.g., Korenaga and Kelemen, 1997). Yet there is evidence that magmatic and hydrothermal activity do occur off-axis. Seafloor mapping reveals venting of hydrothermal fluids at off-axis locales (Haymon et al., 2005) and the ages of some off-axis lavas are anomalously young (Zou et al., 2002; Sims et al., 2003).

Here we present evidence of off-axis crustal magmatism from seismic refraction data (Fig. 1) that constrain the intrusive complex's location, size and physical properties. The seismic experiment used 28 four-component ocean-bottom seismometers (OBSs) and 29 ocean-bottom hydrophones (OBHs) to record rise parallel and perpendicular shooting lines; the source was the 20-gun, 8420 in.^{3} *R/V Ewing* airgun array. Previous analyses of the data constrain regional scale variations in crustal thickness (Canales et al., 2003) and the structure of a mantle-low velocity zone (MLVZ) that is skewed beneath the spreading axis (Toomey et al., 2007).

2. Seismic observations

The off-axis magmatic complex is defined by the following three observations (Fig. 1): (i) *P* waveforms that diffract around a low-velocity body in the mid-crust, (ii) an abrupt attenuation of energy that propagates through the anomalous region and (iii) a large amplitude *P*-to-*S* wave conversion that requires a solid–liquid interface. We first describe each of these waveform anomalies and then present forward modeling results to show that they are consistent with a pronounced low-velocity, high-attenuation crustal anomaly located ~2 km beneath the seafloor.

Anomalous *P* waveforms are observed in data from two instruments, one located north (OBH 16) and the other south (ORB 2) of the crustal magma body (Fig. 1a and b, Supplementary Fig. 1). The record sections in Fig. 1b are aligned by shot number in order to illustrate that the anomalous waveforms occur within a limited geographic region. The character of the observed waveforms is similar to that of diffracted arrivals predicted by waveform modeling of the axial magma chamber (Wilcock et al., 1993). Diffractions occur when a *P* wave turning in the crust encounters a pronounced low-velocity anomaly whose vertical dimension is less than the seismic wavelength, which gives rise to energy that propagates above (*dPa*) and below (*dPb*) the anomalous feature (Fig. 2). Fig. 1b also shows that, at longer ranges, the first-arriving energy (*dPb*) is strongly attenuated.

* Corresponding author. Tel.: +1 541 346 4582; fax: +1 541 346 4692.
E-mail addresses: ddurant@uoregon.edu (D. Troy Durant), drt@uoregon.edu (D.R. Toomey).

0012-821X/$ – see front matter © 2009 Elsevier B.V. All rights reserved.
doi:10.1016/j.epsl.2009.08.003

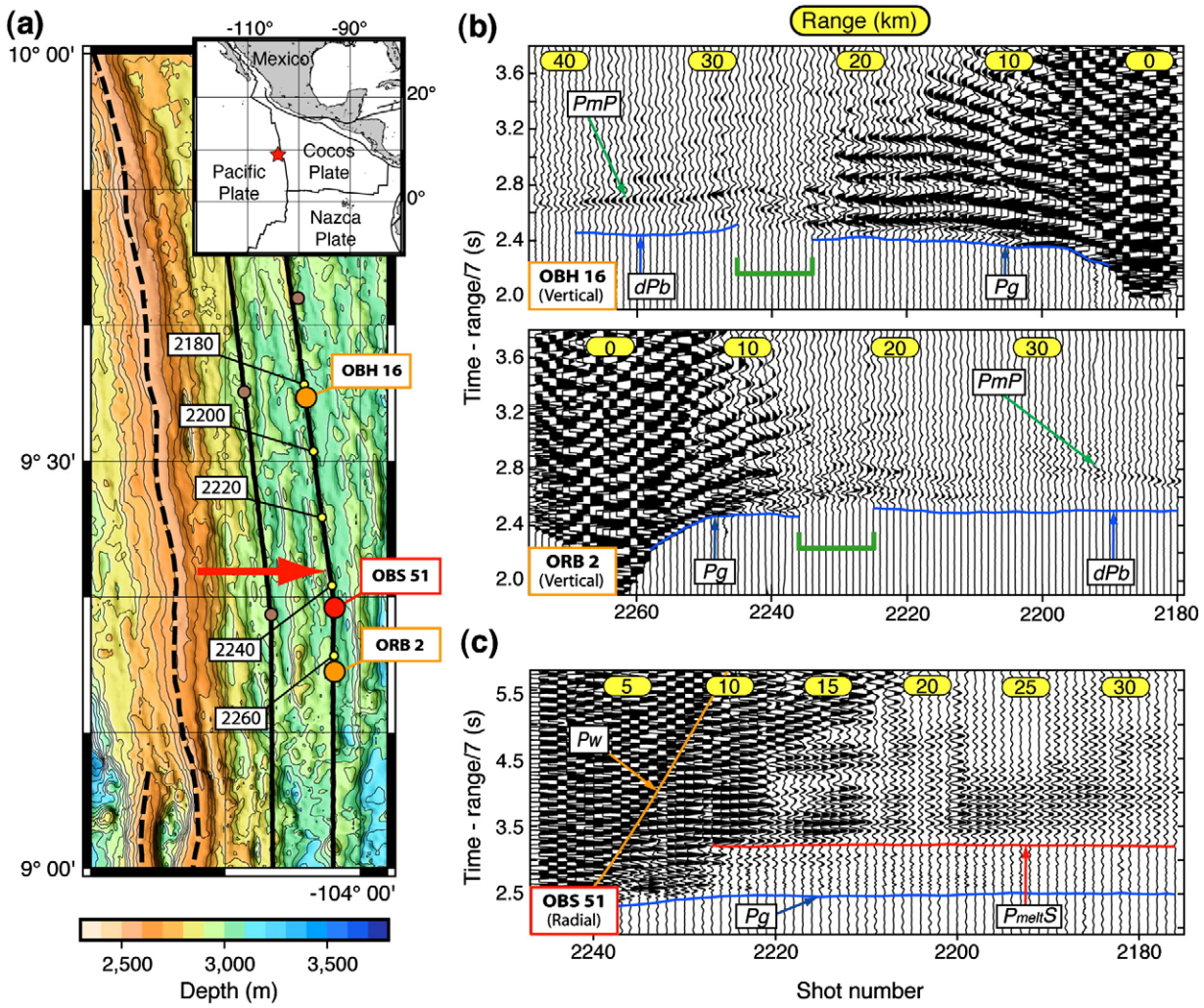

Fig. 1. Map of experimental geometry and seismic record sections. (a) Map of the 9°20′N region of the EPR, showing locations of instruments that recorded *P* wave diffractions (orange circles) and $P_{melt}S$ arrivals (red circle), shown in record sections (b) and (c), respectively. Other instruments in the region are shown as small, brown circles. Shot locations (yellow circles) associated with record sections are labeled. The red arrow points to the center of the magmatic complex's location. Inset shows regional location of study area. (b) Record sections for hydrophones OBH 16 (top) and ORB 2 (bottom), which show diffracted *P* wave arrivals and an abrupt decrease in waveform amplitudes. Record sections are aligned by shot number (bottom axis), ranges are shown in yellow ovals (top axis); amplitudes are fixed scaled. Diffracted *P* wave arrivals are shown by green bar. (c) Radial record section for OBS 51, which shows $P_{melt}S$ (red line). *Pg* (blue line) and *Pw* (water wave; orange line) phases are also shown; amplitudes are fixed scaled. Note the large amplitude of $P_{melt}S$ arrivals out to ranges of 30 km. All record sections are plotted with a velocity reduction of 7 km/s and are band-pass filtered between 5 and 30 Hz.

This energy propagates at mid-crustal depths, which indicates that the anomaly causing the *P* wave diffractions may be underlain by high attenuation crust.

The third observation that defines the crustal magma body is a large amplitude secondary arrival on the radial channel of a seismometer (OBS 51) positioned ~1 km south of the anomaly (Fig. 1a and c). The OBS

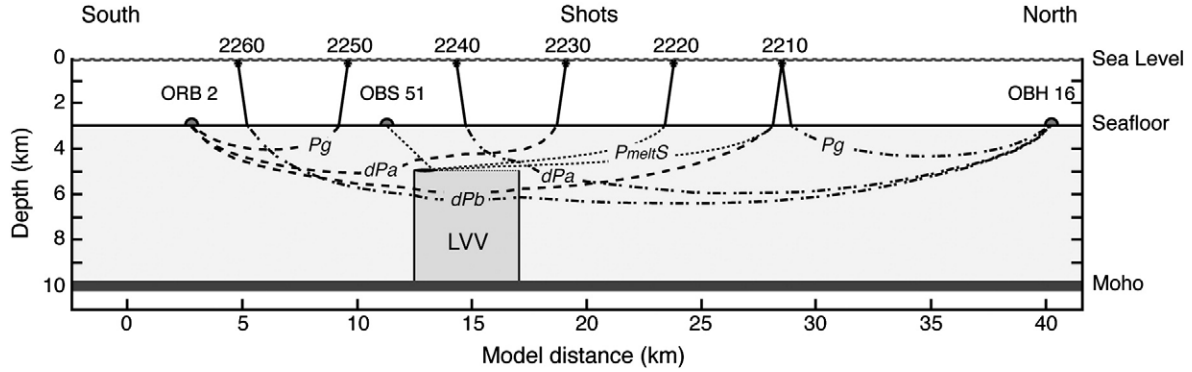

Fig. 2. Source-receiver locations and examples of seismic ray paths. Illustration shows rise-parallel cross-sectional view of crust from south (left) to north (right). Geometry of the LVV with respect to instruments ORB 2, OBS 51 and OBH 16 is roughly to scale. Shot locations along with the region of low velocity and high attenuation below the melt sill are shown. Example ray paths for *Pg*, *dPa* and *dPb* are shown for instruments ORB 2 (dashed line) and OBH 16 (dot-dashed line); $P_{melt}S$ is shown for OBS 51 (dotted line).

orientation was obtained by conducting a particle motion analysis of the direct water wave on horizontal channels; data were subsequently rotated to radial and transverse components. The polarization of the secondary arrival indicates that it is a shear wave, and the character of the phase is consistent with a *P*-to-*S* conversion at a melt lens ($P_{melt}S$) (Garmany, 1989; Singh et al., 1998). The converted phase (Fig. 1c, red line) arrives ~0.7 s after the primary phase *Pg* (Fig. 1c, blue line), and the high-amplitude arrivals are easily observable between 10 and 35 km range north of the receiver. A $P_{melt}S$ phase, however, is not observed south of the receiver (Supplementary Fig. 2, bottom), constraining the reflecting interface to the northern side of OBS 51 in the same region where the *P* wave anomalies are generated.

The pronounced asymmetry observed in the OBS 51 data (Supplementary Fig. 2, bottom) is a unique phenomenon among all of the radial data from the region. A typical radial record section from an OBS (OBS 64), located 20 km east of the rise axis and ~60 km north of OBS 51, is shown in Supplementary Fig. 2 (top) for comparison. We considered the possibility that the high-energy secondary phase observed on the north side is *Ps*, a *P*-to-*S* wave conversion at the base of the upper-most basaltic layer (layer 2A) of the crust (Christeson et al., 1997). This possibility, however, is unlikely for several reasons. In the absence of an abrupt velocity change, the difference in *Ps* arrival times between the north and south sides of OBS 51 would require an increase of 300 m in layer 2A thickness over a lateral distance of less than 1 km. The 0.7-second time difference between *Pg* and *P*-to-*S* wave arrivals on the north side would require a layer 2A thickness of ~800 m as well, which is inconsistent with previous studies of this region (Bazin et al., 2001). Moreover, the *T*–*X* curve (arrival time with respect to range) for *Ps* parallels that of *Pg*, but the *T*–*X* curve for the high-amplitude phase on the north side of OBS 51 diverges from *Pg* at close range (Supplementary Fig. 2, bottom). As range decreases below 10 km, the *T*–*X* curve for the high-amplitude phase monotonically increases in a hyperbolic manner, which is characteristic of a reflected phase. There is also subtle evidence of low-amplitude *Ps* arrivals observed on the north side of OBS 51 with similar arrival times as those to the south, which suggests that the crustal anomaly may be affecting the generation of *Ps* to the north of the OBS.

3. Seismic modeling

We use travel time (Toomey et al., 1994), and finite difference waveform (Levander, 1988; Larsen and Harris, 1993) modeling to determine the geometry and physical properties of the crustal anomaly. Two-dimensional finite difference models consist of a 50-km-long, rise-parallel cross-section that includes a 3-km-deep water layer, 7-km-thick crust, 1-km-thick Moho transition zone (MTZ) and 3-km-thick upper mantle region. Embedded in the crust is a low-velocity volume (LVV) that includes a 100-m-thick sill with low shear modulus atop a low-velocity region extending to the base of the crust (Fig. 3a, Supplementary Fig. 3; see Appendix A). We perform over 50 separate forward modeling experiments where we vary the length, depth and physical properties of the LVV in order to find a model whose resultant waveform anomalies are comparable to the actual data. Synthetic data from stations S1, S2 and S3 (Fig. 3) are selected for comparison with ORB 2, OBS 51 and OBH 16 data (Fig. 1), respectively. Waveform data from a model without an LVV are shown for comparison (Fig. 3b and c, bottom).

4. Modeling results

The observed *P* wave diffractions fix the location, length and average velocity of the LVV. Modeling results show that as the depth of the LVV increases, the range between the receiving station and the observed split in *Pg* energy increases, and waveform diffractions become more difficult to identify. No *P* wave diffractions are observed when the LVV is modeled at depths of 4 km or more. Modeling results further show that the time difference between *Pg* and *dPb* arrivals is sensitive to the velocity beneath the melt sill (i.e., the underlying LVV). Synthetic vertical record sections for S1 and S3 (Fig. 3b), aligned by shot number, show evidence for *P* wave diffractions similar to those observed in ORB 2 and OBH 16 data when we use a 4.5-km-long LVV that begins 2 km below the seafloor (Fig. 3a).

We presume in our model that the sudden decrease in waveform amplitude that is observed in ORB 2 and OBH 16 data (Fig. 1b) is a result of increased crustal attenuation. We estimate the degree of attenuation by comparing synthetic and observed waveform amplitudes. ORB 2 and OBH 16 data consistently show a smaller average for first-arrival amplitudes at post-anomaly ranges compared to similar ranged arrivals on the opposite side of each receiver. Waveform modeling confirms that an LVV with an attenuation anomaly in the mid- to lower-crust decreases the amplitude of both first and secondary arrivals. Synthetic data (Fig. 3b) are comparable to ORB 2 and OBH 16 data when the attenuating region is modeled with quality factor (Q) values between 30 and 70, which is an order of magnitude less than Q values for normal, off-axis oceanic crust at similar depths (Wilcock et al., 1992).

The high amplitude *S* wave arrival observed on the radial channel of OBS 51 constrains the physical properties of a sill located at the top of the LVV. The amplitude and observable range of *P*-to-*S* reflections are primarily sensitive to the shear modulus (μ) of the medium below the reflecting interface. An energy coefficient versus incident angle analysis indicates efficient *P*-to-*S* wave conversion occurs at a solid–liquid interface (Supplementary Fig. 4). At wide angles (or large offsets), ~50% of the *P* wave's energy is reflected as an *S* wave, since no *S* wave energy is transmitted into the liquid.

Waveform modeling confirms that a finite-length sill also generates large amplitude *P*-to-*S* arrivals. Fig. 3c (top) shows high-amplitude *P*-to-*S* arrivals (labeled $P_{melt}S$) on the radial channel for synthetic station S2, which is located ~1 km from a fluid-filled sill (Fig. 3a). We use the term "$P_{melt}S$" to include both specular and diffracted reflections. The converted *S* wave appears at ranges of ~5 to more than 30 km; this is true for all of our models that contain a crustal melt lens, regardless of lens depth. When the lens is semi-rigid or mush-like, reflection amplitudes drop significantly. We thus attribute the large amplitude arrival observed on the radial channel of OBS 51 to a *P*-to-*S* conversion from a sill with zero or near-zero shear modulus. Modeling results also show that the time difference between *Pg* and $P_{melt}S$, as well as the appearance of $P_{melt}S$ at close range (<5 km), constrain the depth to the top of the sill. As sill depth increases, so does the *Pg*-$P_{melt}S$ time difference, and $P_{melt}S$ at close range becomes more visible as its energy separates from that of the water wave. A comparable fit between S2 and OBS 51 data occurs when we model a sill at 2 km depth.

We investigate layer 2A waveform effects, both with and without a melt sill, to determine if either *Ps* or any multiple phases (e.g., *PP* and *PPs*) appear similar to $P_{melt}S$ (Supplementary Fig. 5). These phases are created when a velocity discontinuity between layers 2A and 2B is added to our waveform models. As noted above, $P_{melt}S$ results when a melt sill is present, and Supplementary Fig. 5 (bottom) shows that its associated *T*–*X* curve hyperbolically increases while diverging from *Pg* as range decreases (<10 km). The *T*–*X* curve for *Ps*, however, parallels that of *Pg*, and, in the melt sill model, *Ps* becomes highly attenuated at ranges beyond 10 km. These results correlate well with the OBS 51 data. When no melt sill is present, *Ps* is easily observed out to ranges beyond 30 km (Supplementary Fig. 5, top). The T–X curvature for *P* wave (*PP*) and converted *P*-to-*S* wave (*PPs*) multiples is similar to that of *Pg* and *Ps*, which distinguishes these phases from $P_{melt}S$ as well.

5. Discussion and conclusions

On the basis of our modeling, we conclude that a seismic velocity and attenuation anomaly located ~20 km east of the rise is the result of a crustal-level magmatic complex. The simplest structure consistent with

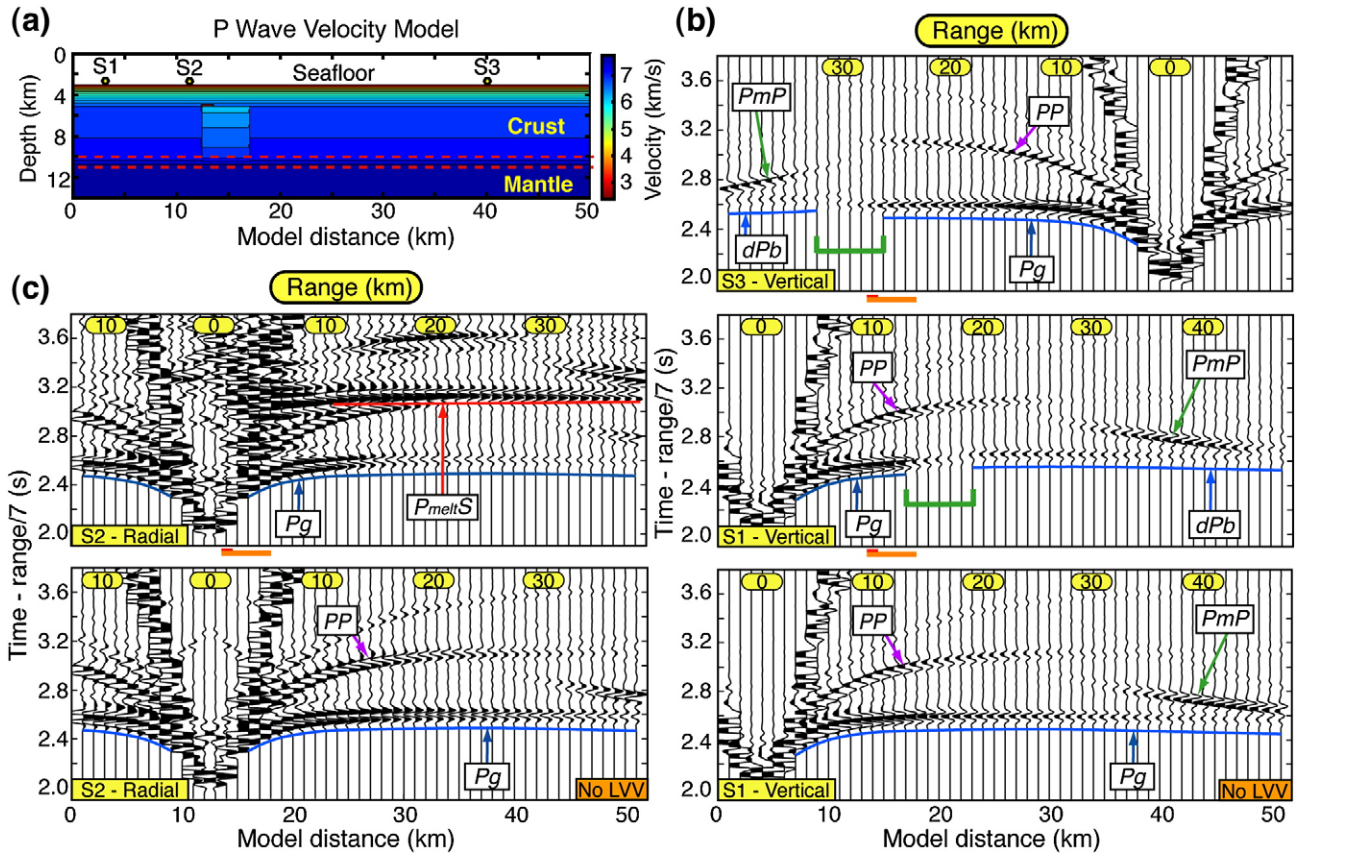

Fig. 3. Finite difference model and synthetic record sections. (a) *P* wave velocity model with embedded LVV beginning 2 km below the seafloor. Yellow circles show synthetic station locations (S1–S3) associated with record sections shown in (b) and (c). (b) Synthetic vertical record sections for stations S1 (middle) and S3 (top) showing *P* wave diffractions and attenuated arrivals. Diffracted *P* wave arrivals are shown by green bar. A synthetic vertical record section for station S1 (bottom) from a model without an LVV is shown for comparison. *PP* and *PmP* phases are also shown in each record section. Orange bar along bottom axes of record sections indicates LVV's position in the model space; red bar shows the sill location. (c) Synthetic radial record sections for station S2 from models with (top) and without (bottom) an embedded LVV. High-amplitude $P_{melt}S$ arrivals (red line) are observed at ranges of ~5 to more than 30 km when a sill is present. All record sections are plotted with a velocity reduction of 7 km/s and are band-pass filtered between 5 and 30 Hz.

our data is a 1-km-long (±0.5 km) melt sill located at a depth of 2 km beneath the seafloor that is underlain by a broader region (4.5-km-long, ±1 km) of crust that is anomalously hot and perhaps partially molten. The exact degree of attenuation within the LVV is difficult to resolve because of its limited spatial extent, nevertheless our *Q* estimates do indicate an order of magnitude increase in attenuation compared to normal, off-axis crustal values. We note that the LVV was not detected in a previous two-dimensional tomographic study of the region (Canales et al., 2003). The limited spatial extent of the LVV allows for rapid, post-anomaly wavefront healing, which results in a travel-time effect for first arrivals that is not large (<50 ms) and that is limited to a small number of shots. This makes the anomaly difficult to resolve by delay-time tomographic methods. Our results indicate that waveform data can better reveal crustal magma bodies such as the one we have found, particularly when compared to a two-dimensional tomographic study.

The high-attenuation LVV we detect is consistent with the injection of a significant amount of heat into the ridge flank. If the cross-axis width of the anomaly is only 1 km, we conservatively estimate ~1×10^{19} J of anomalous heat has been supplied to the crust compared to average off-axis mid- to lower-crustal reference temperatures between 400 and 800 °C (see Appendix B). The latent heat of crystallization associated with a single melt sill like the one in our model accounts for less than 2% of the estimated heat. We thus conclude that the high-attenuation LVV marks a site of repeated intrusive activity.

We attribute the occurrence of repeated, off-axis magmatic activity to a long-lived skew between the axes of mantle upwelling and plate spreading (Toomey et al., 2007; Toomey and Hooft, 2008) (Fig. 4). As a consequence of this skew the MLVZ – which defines the pattern of magma delivery from the mantle to the crust – is offset to the east of the rise, roughly underlying the high-attenuation, crustal-level LVV. Analyses of bathymetry, seismic crustal thickness and gravity data indicate that a skewed pattern of mantle upwelling has persisted in this region for at least 1 Ma (Toomey and Hooft, 2008). In addition, where we have imaged a crustal magmatic intrusion, both the MTZ (Vera et al., 1990) and the crust (Canales et al., 2003) are anomalously thick and the average crustal density is elevated (Canales et al., 2003, Toomey and Hooft, 2008). We thus infer that the off-axis delivery of mantle melt gives rise to magmatic underplating and intrusive activity that thickens both the MTZ and the crust, thereby fundamentally altering crustal architecture (Fig. 4). Our discovery of off-axis magmatic activity may thus explain the large number of crosscutting dikes, sills and intrusions of ultra-mafic and mafic composition in the crust as observed in the Oman ophiolite complex (Juteau et al., 1988; Nicolas et al., 1996). In regions of the ophiolite complex where there is a thick Moho, wehrlitic intrusions are found in every level of the crustal section, and it is estimated that they can make up as much as 20 to 40% of the total volume of the crustal plutonic sequence (Juteau et al., 1988).

Repeated intrusive activity may act as a source for off-axis lava flows and drive off-axis hydrothermal circulation (Fig. 4). Although there are no currently known bathymetric or morphologic features that indicate extrusive volcanism immediately above the magma body we image, anomalously young lavas have been found nearby (Zou et al., 2002). Off-axis hydrothermal activity is likely dominated by diffuse flow venting, although focused, high-temperature vents (i.e., black smokers) near shallow-crustal magma bodies could be present. Deep crustal penetration of seawater through fractures and microcracks (Nicolas and

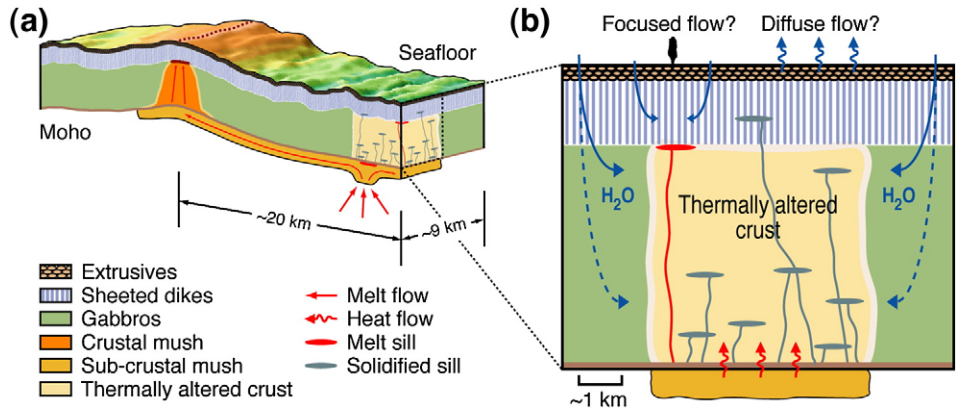

Fig. 4. Crustal alteration due to the off-axis delivery of mantle melt. (a) Perspective view of study area (right side) with respect to the ridge axis (dotted red line); bathymetry is exaggerated. Diagram shows an area of thermally altered crust (tan region) associated with the off-axis delivery of mantle melt. Melt migration (solid red arrows) toward the rise axis likely occurs at sub-Moho depths within a mushy layer (orange region). (b) Close-up of the rise-parallel crustal face associated with the results of our study. Diagram shows a region of crust that has been thermally altered due to the release of heat from crystallizing sub-crustal melt (wavy red arrows) as well as solidifying crustal intrusions (gray ellipses). Blue arrows illustrate possible upper-crustal (solid) and deep-crustal (dashed) penetration of seawater. High-temperature vents (black cloud) may be generated by focused hydrothermal flow near shallow magma bodies like the one we detect (red ellipse), but diffuse flow venting (wavy blue arrows) likely dominates the thermally altered region.

Mainprice, 2005) also provides a mechanism for driving off-axis wehrlite formation (Feig et al., 2006). Hydrothermal venting, whether focused or diffuse, would produce a chemically life-sustainable environment for biological communities to thrive at off-axis locales. Our results provide compelling motivation for expanding the search for seafloor hydrothermal activity and its associated ecosystems beyond the axis of seafloor spreading.

Acknowledgements

We thank Shawn Larsen at Lawrence Livermore National Laboratory for his help with utilizing E3D (finite difference software) and Donald Forsyth for his comments. This work was supported by the RIDGE and RIDGE 2000 Programs as well as NSF grants OCE-0732751, OCE-0118597, OCE-9633264 and EAR-0651123.

Appendix A. Waveform model parameterization

We use E3D, an explicit 2D/3D elastic finite difference wave propagation code that is 4th-order accurate in space and 2nd-order accurate in time, for our finite difference modeling (Levander, 1988; Larsen and Harris, 1993). The finite difference crustal model consists of a 5001×1401 nodal grid with a 10 m nodal spacing in the horizontal and vertical directions (50×14 km^2). Absorbing boundary conditions are used on the sides and bottom and a free surface boundary condition at the top. Some reflecting energy, however, remains within the model space. To further reduce boundary effects, we add additional nodes to the sides and bottom that make the overall model dimensions 7001×2001 nodes (70×20 km^2) (Supplementary Fig. 3a). We place a 5-km-wide high attenuation ($Q=5$) boundary along the sides and bottom as well (Supplementary Fig. 1b). Topography is excluded from the model. For most models, the layer 2A–2B velocity discontinuity is replaced by a continuous gradient in order to remove the many converted phases that are outside the scope of our study. Crustal Vp/Vs ratios and Q values are slightly modified from Vera et al. (1990) and Wilcock et al. (1992), respectively (Supplementary Fig. 3), and crustal densities (ρ) are calculated using the density–velocity relationship $\rho=0.165Vp+1.852$ (Christensen and Shaw, 1970). The source consists of a Ricker wavelet with a center frequency of 10 Hz. Shots (1 per run) are spaced at 1 km intervals and begin 10 m below sea level. We perform 51 separate runs for each synthetic model (one for each shot position) in order to construct record sections that are comparable to data. Synthetic data are band-pass filtered between 5 and 30 Hz.

Appendix B. Heat calculations

We estimate the amount of heat being injected into the ridge flank by calculating the amount of heat required to generate the velocity anomaly observed in our seismic data. We use the velocity and attenuation results from our modeling and add a 1-km-width to our LVV. We begin with the temperature derivative of seismic velocity κ (Karato, 1993),

$$\kappa = \frac{\partial lnV}{\partial T} = \frac{\partial lnV_0}{\partial T} - F(\alpha)\left(\frac{Q^{-1}(\omega,T)}{\pi}\right)\left(\frac{H^*}{RT^2}\right). \quad (1)$$

where V_0 is a reference velocity corresponding to the unrelaxed state of the medium, Q^{-1} is the reciprocal of the quality factor, ω is frequency, T is temperature, H^* is activation enthalpy, R is the gas constant and $F(\alpha)=(\pi\alpha/2)\cot(\pi\alpha/2)$ where α is the exponent of the power law dependence of Q on frequency ($Q\sim\omega^{\alpha}$). The first term in this equation represents anharmonic effects (no seismic energy loss), and the second term represents anelastic effects (entails seismic energy loss). Anelasticity can significantly increase the temperature derivative, thereby reducing the thermal anomaly required to generate the observed velocity anomaly. To obtain a minimum value for the thermal anomaly, we maximize the effects of anelasticity by setting $F(\alpha)=1$. We use a value of -8.1×10^{-5} K^{-1} for the anharmonic term (Christensen, 1979), and use the following values for the remaining variables: $Q^{-1}=0.02$ (a viable estimate from our modeling results), $H^*=276$ kJ mol^{-1} (Caristan, 1982)) and $R=8.314$ J mol^{-1} K^{-1}. For T, we use 400, 600 and 800 °C, which is a range of average mid-crustal temperatures expected for normal off-axis crust (Dunn et al., 2000; Maclennan et al., 2005). Using these values in Eq. (1) gives us the following solutions for κ_n, where $n=400$, 600 and 800: $\kappa_{400}=-5.47\times10^{-4}$ K^{-1}, $\kappa_{600}=-3.58\times10^{-4}$ K^{-1} and $\kappa_{800}=-2.65\times10^{-4}$ K^{-1}. Supplementary Fig. 6a shows that the magnitude of κ decreases with increasing Q as anelastic effects diminish.

To determine the temperature anomaly associated with each value of κ, we use the relation

$$\partial V_p = \kappa Vp\,\partial T. \quad (2)$$

We estimate the derivatives in Eq. (2) by using Δ and rearrange the equation to get

$$\Delta T_n = \frac{\Delta Vp}{\kappa_n Vp_{\text{crust}}} \quad (n = 400, 600, 800). \tag{3}$$

ΔVp ($\Delta Vp = -0.3$ km s^{-1}) is determined by taking the average of the velocity values within the modeled LVV ($Vp_{\text{LVV}} = 6.7$ km s^{-1}) and comparing it to the average mid- to lower-crustal velocity value near OBS 51 ($Vp_{\text{crust}} = 7.0$ km s^{-1}) (Canales et al., 2003). Using our values for κ_n and ΔVp, we get the following solutions for ΔT_n: $\Delta T_{400} = 78$ °C, $\Delta T_{600} = 120$ °C and $\Delta T_{800} = 162$ °C. These ΔT values assume a Q value of 50 everywhere, however Supplementary Fig. 6b shows that as Q increases the thermal anomaly required to generate the observed velocity anomaly also increases.

We calculate the amount of heat (Q_{heat}) required to generate the temperature anomaly within the LVV using the standard heat equation,

$$Q_{\text{heat}}(n) = m_{\text{LVV}} Cp_n \Delta T_n \quad (n = 400, 600, 800), \tag{4}$$

where m_{LVV} is the mass of the rock within the LVV, Cp_n is the specific heat capacity of the rock at constant pressure and ΔT_n is change in temperature. Using the density of gabbro ($\rho_{\text{gabbro}} = 2970$ kg m^{-3}) (Waples and Waples, 2004) and an LVV volume of 22.5 km^3 (4.5 km L × 5 km H × 1 km W), we get $m_{\text{LVV}} = 6.7 \times 10^{13}$ kg. Because specific heat capacity is temperature dependent, we use the method of Waples and Waples (2004) to calculate values for Cp_n. The regression equation

$$Cp_{n_T} = 8.95 \times 10^{-10} T^3 - 2.13 \times 10^{-6} T^2 + 0.00172T + 0.716 \tag{5}$$

gives us a normalized heat capacity of a mineral or nonporous rock at any temperature T (°C). As long as a measured value for the specific heat capacity (Cp_{T1}) is available for the rock or mineral at any given temperature T_1, then Eq. (6) can be used to calculate the theoretical specific heat capacity (Cp_{T2}) for the same rock or mineral at a new temperature T_2:

$$Cp_{T_2} = Cp_{T_1} \left(\frac{Cp_{n_{T_2}}}{Cp_{n_{T_1}}} \right). \tag{6}$$

We thus obtain the following values for the specific heat capacity of gabbro (Cp_n), where the measured value for gabbro is 1000 J kg^{-1} K^{-1} at 20 °C (Waples and Waples, 2004): $Cp_{400} = 1495$ J kg^{-1} K^{-1}, $Cp_{600} = 1567$ J kg^{-1} K^{-1} and $Cp_{800} = 1584$ J kg^{-1} K^{-1}. Using our values for m_{LVV}, Cp_n and ΔT_n in Eq. (4) gives us the following solutions for heat: $Q_{\text{heat}}(400) = 7.5 \times 10^{18}$ J, $Q_{\text{heat}}(600) = 1.2 \times 10^{19}$ J and $Q_{\text{heat}}(800) = 1.6 \times 10^{19}$ J. From these solutions, we use an estimate of 1×10^{19} J for the amount of heat being injected into the ridge flank at our study site. Supplementary Fig. 6c illustrates that the amount of heat required to generate a specific velocity anomaly increases with respect to increasing Q, thus our heat estimate via a Q value of 50 is rather conservative. Similar analyses using velocity anomalies (ΔVp) of −0.2 and −0.1 km s^{-1} for comparison yield a reduction in heat values of 33 and 66%, respectively.

To estimate the heat contributed by a single melt sill, like the one in our model, we calculate the amount of heat given off during sill solidification. We use a value of 5.0×10^5 J kg^{-1} for the latent heat of crystallization for basaltic melts in the crust (Cannat et al., 2004). A melt density of 2600 kg m^{-3} and a sill volume of 0.1 km^3 (1 km L × 0.1 km H × 1 km W) yields a mass for the melt sill of 2.60×10^{11} kg. If the sill were to totally crystallize, it would generate ~1.3×10^{17} J of heat (latent heat of crystallization × mass), which is less than 2% of the estimated heat required to generate the observed LVV.

Appendix C. Supplementary data

Supplementary data associated with this article can be found, in the online version, at doi:10.1016/j.epsl.2009.08.003.

References

Bazin, S., Harding, A.J., Kent, G.M., Orcutt, J.A., Tong, C.H., Pye, J.W., Singh, S.C., Barton, P.J., Sinha, M.C., White, R.S., Hobbs, R.W., Van Avendonk, H.J.A., 2001. Three-dimensional shallow crustal emplacement at the 9°03′N overlapping spreading center on the East Pacific Rise: Correlations between magnetization and tomographic images. J. Geophys. Res. 106, 16101–16117.

Canales, J.P., Detrick, R.S., Toomey, D.R., Wilcock, W.S.D., 2003. Segment-scale variations in the crustal structure of 150–300 kyr old fast spreading oceanic crust (East Pacific Rise, 8°15′N–10°5′N) from wide-angle seismic refraction profiles. Geophys. J. Int. 152, 766–794.

Cannat, M., Cann, J., Maclennan, J., 2004. Some hard rock constraints on the supply of heat to mid-ocean ridges. In: German, C.R., Lin, J., Parson, L.M. (Eds.), Mid-Ocean Ridges: Hydrothermal Interactions Between the Lithosphere and Oceans. Geophysical Monograph, 148. American Geophysical Union, pp. 111–149.

Caristan, Y., 1982. The transition from high temperature creep to fracture in Maryland diabase. J. Geophys. Res. 87, 6781–6790.

Christensen, N.I., 1979. Compressional wave velocities in rocks at high temperatures and pressures, critical thermal gradients, and crustal low-velocity zones. J. Geophys. Res. 84, 6849–6857.

Christensen, N.I., Shaw, G.H., 1970. Elasticity of mafic rocks from the Mid-Atlantic Ridge. Geophys. J. Int. 20, 271–284.

Christeson, G.L., Shaw, P.R., Garmany, J.D., 1997. Shear and compressional wave structure of the East Pacific Rise, 9°–10° N. J. Geophys. Res. 102, 7821–7835.

Detrick, R.S., Buhl, P., Vera, E., Mutter, J., Orcutt, J., Madsen, J., Brocher, T., 1987. Multi-channel seismic imaging of a crustal magma chamber along the East Pacific Rise. Nature 326, 35–41.

Dunn, R.A., Toomey, D.R., Solomon, S.C., 2000. Three-dimensional seismic structure and physical properties of the crust and shallow mantle beneath the East Pacific Rise at 9°30′N. J. Geophys. Res. 105, 23537–23555.

Feig, S.T., Koepke, J., Snow, J.E., 2006. Effect of water on tholeiitic basalt phase equilibria: an experimental study under oxidizing conditions. Contrib. Mineral. Petrol. 152, 611–638.

Fornari, D.J., Haymon, R.M., Perfit, M.R., Gregg, T.K.P., Edwards, M.H., 1998. Axial summit trough of the East Pacific Rise 9°–10°N: geological characteristics and evolution of the axial zone on fast spreading mid-ocean ridges. J. Geophys. Res. 103, 9827–9855.

Garmany, J., 1989. Accumulations of melt at the base of young oceanic crust. Nature 340, 628–632.

Haymon, R.M., Fornari, D.J., Edwards, M.H., Carbotte, S., Wright, D., Macdonald, K.C., 1991. Hydrothermal vent distribution along the East Pacific Rise crest (9°09′–54′N) and its relationship to magmatic and tectonic processes on fast-spreading mid-ocean ridges. Earth Planet. Sci. Lett. 104, 513–534.

Haymon, R.M., Macdonald, K.C., Benjamin, S.B., Ehrhardt, C.J., 2005. Manifestations of hydrothermal discharge from young abyssal hills on the fast-spreading East Pacific Rise flank. Geology 33, 153–156.

Juteau, T., Ernewein, M., Reuber, I., Whitechurch, H., Dahl, R., 1988. Duality of magmatism in the plutonic sequence of the Sumail Nappe, Oman. Tectonophysics 151, 107–135.

Karato, S., 1993. Importance of anelasticity in the interpretation of seismic tomography. Geophys. Res. Lett. 20, 1623–1626.

Kent, G.M., Harding, A.J., Orcutt, J.A., 1990. Evidence for a smaller magma chamber beneath the East Pacific Rise at 9°30′N. Nature 344, 650–653.

Korenaga, J., Kelemen, P.B., 1997. Origin of gabbro sills in the Moho transition zone of the Oman ophiolite: implications for magma transport in the oceanic lower crust. J. Geophys. Res. 102, 27729–27749.

Larsen, S., Harris, D., 1993. Seismic wave propagation through a low-velocity nuclear rubble zone. Lawrence Livermore Natl. Lab. Tech. Rep. UCRL-ID-115729.

Levander, A., 1988. Fourth-order finite-difference P-SV seismograms. Geophysics 53, 1425–1436.

Macdonald, K.C., Fox, P.J., 1988. The axial summit graben and cross-sectional shape of the East Pacific Rise as indicators of axial magma chambers and recent volcanic eruptions. Earth Planet. Sci. Lett. 88, 119–131.

Maclennan, J., Hulme, T., Singh, S.C., 2005. Cooling of the lower oceanic crust. Geology 33, 357.

Nicolas, A., Mainprice, D., 2005. Burst of high-temperature seawater injection throughout accreting oceanic crust: a case study in Oman ophiolite. Terra Nova 17, 326–330.

Nicolas, A., Boudier, F., Ildefonse, B., 1996. Variable crustal thickness in the Oman ophiolite: implication for oceanic crust. J. Geophys. Res. 101, 17941–17950.

Sims, K.W.W., Blichert-Toft, J., Fornari, D.J., Perfit, M.R., Goldstein, S.J., Johnson, P., DePaolo, D.J., Hart, S.R., Murrell, M.T., Michael, P.J., Layne, G.D., Ball, L.A., 2003. Aberrant youth: chemical and isotopic constraints on the origin of off-axis lavas from the East Pacific Rise, 9°–10° N. Geochem. Geophys. Geosyst. 4, 8621. doi:10.1029/2002GC000443.

Singh, S.C., Kent, G.M., Collier, J.S., Harding, A.J., Orcutt, J.A., 1998. Melt to mush variations in crustal magma properties along the ridge crest at the southern East Pacific Rise. Nature 394, 874–878.

Toomey, D.R., Hooft, E.E.E., 2008. Mantle upwelling, magmatic differentiation, and the meaning of axial depth at fast-spreading ridges. Geology 36, 679–682.

Toomey, D.R., Solomon, S.C., Purdy, G.M., 1994. Tomographic imaging of the shallow crustal structure of the East Pacific Rise at 9°30′N. J. Geophys. Res. 99, 24135–24157.
Toomey, D.R., Jousselin, D., Dunn, R.A., Wilcock, W.S.D., Detrick, R.S., 2007. Skew of mantle upwelling beneath the East Pacific Rise governs segmentation. Nature 446, 409–414.
Vera, E.E., Mutter, J.C., Buhl, P., Orcutt, J.A., Harding, A.J., Kappus, M.E., Detrick, R.S., Brocher, T.M., 1990. The structure of 0- to 0.2-m.y.-old oceanic crust at 9°N on the East Pacific rise from expanded spread profiles. J. Geophys. Res. 95, 15529–15556.
Waples, D.W., Waples, J.S., 2004. A review and evaluation of specific heat capacities of rocks, minerals, and subsurface fluids. Part 1: Minerals and nonporous rocks. Nat. Resour. Res. 13, 97–122.
Wilcock, W.S.D., Solomon, S.C., Purdy, G.M., Toomey, D.R., 1992. The seismic attenuation structure of a fast-spreading mid-ocean ridge. Science 258, 1470–1474.
Wilcock, W.S.D., Dougherty, M.E., Solomon, S.C., Purdy, G.M., Toomey, D.R., 1993. Seismic propagation across the East Pacific Rise: finite difference experiments and implications for seismic tomography. J. Geophys. Res. 98, 19913–19932.
Zou, H., Zindler, A., Niu, Y., 2002. Constraints on melt movement beneath the East Pacific Rise from ^{230}Th–^{238}U disequilibrium. Science 295, 107–110.